Bulk versus Spectral Wave Parameters: Implications on Stokes Drift Estimates, Regional Wave Modeling, and HF Radars Applications

NIRNIMESH KUMAR

Department of Civil and Environmental Engineering, University of Washington, Seattle, Washington

DOUGLAS L. CAHL

School of the Earth, Ocean and Environment, University of South Carolina, Columbia, South Carolina

SEAN C. CROSBY

Integrative Oceanography Division, Scripps Institution of Oceanography, La Jolla, California

GEORGE VOULGARIS

School of the Earth, Ocean and Environment, University of South Carolina, Columbia, South Carolina

(Manuscript received 2 September 2016, in final form 8 February 2017)

ABSTRACT

Accurate estimates of Stokes drift are necessary to quantify Lagrangian transport and upper-ocean mixing. These can be estimated from directional wave spectra. Here, a methodology for the reconstruction of such spectra is developed using partitioned bulk wave parameters provided by global wave models. These reconstructed spectra agree well with global wave model–simulated full spectra. Regional wave model simulations with reconstructed spectra as open boundary conditions lead to more accurate estimates of bulk wave parameters in the coastal ocean. Furthermore, the reconstructed directional spectra can be used to improve high-frequency (HF) radar–derived surface Lagrangian current estimates. Stokes drift vertical profiles from complete directional spectra are more accurate, and therefore coupled ocean circulation and wave models should incorporate spectral estimates for wave–current interaction studies. Based on model simulations conducted here, it is recommended that regional wave modeling studies use partitioned rather than bulk wave parameter products from global wave simulations to reconstruct complete directional spectra for open boundary conditions. Finally, this study shows that inclusion of the peak spectral energy for each partition improves the ability to reconstruct more accurately directional spectra and surface Stokes drift. It is recommended that the global wave model hindcast/forecast include this additional bulk parameter.

1. Introduction

Surface gravity waves are important drivers for coastal circulation and upper open-ocean mixing. Wave-induced mass flux (i.e., Stokes drift u^{St}; Stokes 1847) affects multiple processes in the marine environment. In an alongshore uniform bathymetry, Stokes drift–induced mass flux leads to offshore-directed undertow in the surfzone

and the inner shelf (e.g., Lentz et al. 2008). Stokes drift and mean velocity shear interaction (i.e., vortex force; Craik and Leibovich 1976) generates Langmuir circulation cells responsible for upper-ocean Langmuir turbulence (e.g., Tejada-Martínez and Grosch 2007; D'Asaro 2014). Accurate Stokes drift estimates are required to determine Lagrangian velocities, which influence dispersion and fate of pollutants, including oil (e.g., Broström et al. 2011), or biological organisms (e.g., larval dispersal; Röhrs et al. 2014). Stokes drift is strongly sheared in the vertical (Breivik et al. 2016), and near the ocean surface typically accounts for two-thirds of the wind-induced drift (Rascle et al. 2008). As direct Stokes drift measurement is challenging (Webb and Fox-Kemper 2015), numerical

estimates are often used in Lagrangian transport. Coupled ocean circulation and wave generation/propagation models (Uchiyama et al. 2010; Warner et al. 2010; Kumar et al. 2012; Ardhuin et al. 2008; Bennis et al. 2011; Moghimi et al. 2013) estimate Stokes drift to quantify wave–current interaction. The Stokes drift vertical structure depends on the directional wave spectra (Kenyon 1969); however, in most of the aforementioned models, Stokes drift is estimated using bulk wave parameters (significant wave height H_s, peak period T_p, and mean direction θ_m). The difference in Stokes drift estimates from directional wave spectra versus bulk wave parameters is considered for multimodal and multidirectional seas in appendix A.

The choice between bulk wave parameters and directional wave spectrum is also important as boundary forcing for regional wave propagation model simulations. Bulk wave parameters from global wave model hindcast/forecast [e.g., WAVEWATCH III (WW3); Tolman 2009; Chawla et al. 2013; Rascle and Ardhuin 2013] are often used as the boundary condition for regional coupled ocean circulation and wave modeling studies (e.g., Warner et al. 2010; Olabarrieta et al. 2012; Hopkins et al. 2016). This simplification, especially in multimodal seas, leads to prediction errors in the evolution of the sea state, bulk wave parameters, Stokes drift, and radiation stresses, especially in the nearshore and regions with extensive wave sheltering [e.g., Southern California Bight (SCB); Crosby et al. 2016]. Although global wave models internally calculate the complete directional wave spectrum, that is, $S_{\eta\eta}(f, \theta)$, only total bulk and partitioned bulk wave parameters are saved at each grid location in order to reduce storage requirements.

Complete directional wave spectra $S_{\eta\eta}(f, \theta)$ estimated from directional buoy observations are available at various locations around the United States and elsewhere. Directional spectra estimates from buoys observations, though nonunique (Ochoa and Delgado-González 1990) and not without statistical uncertainty (Crosby et al. 2016), are relatively accurate as evident in their effective use for nearshore wave prediction (O'Reilly et al. 2016) and can be used to make good Stokes drift estimates. However, the spatial distribution of buoy observations is not sufficient to provide adequate wave boundary conditions for relatively large-scale (10^2–10^3 km), regional, coupled ocean circulation and wave model simulations or to estimate Stokes drift with sufficient spatial resolution. On the other hand, large-scale, near-surface Lagrangian (i.e., Eulerian mean + Stokes drift) current estimates are routinely obtained through the use of high-frequency (HF) radars (Harlan et al. 2010). These current estimates can be assimilated into numerical models (e.g., Paduan and Shulman 2004; Breivik and Sætra 2001), improving

overall model performance at regional scales. Even HF radar–derived currents include only a part of the total Stokes drift that is a function of the radar operating frequency (e.g., Ardhuin et al. 2009). These current estimates must be adjusted to account for the missing part of the Stokes drift (Cahl and Voulgaris 2016) that depends on the high-order details of local wave conditions, that is, the full directional wave spectrum. The latter can be provided at the spatial resolution of HF radar velocity estimates only through the use of regional wave models.

Given the importance of directional wave spectra for a variety of nearshore applications, we have developed a methodology to reconstruct complete $S_{\eta\eta}(f, \theta)$ from WW3 or any other global wave model that provides partitioned bulk wave parameters. The objective of this study is to investigate the implications of using spectral versus bulk wave parameters on Stokes drift estimates, regional wave modeling, and HF radar Lagrangian current estimates. In section 2, the directional wave spectrum reconstruction methodology is presented. Section 3 demonstrates the reconstruction method skill in defining wave boundary conditions for regional wave model applications. Section 4 demonstrates the reconstruction methods skill for improving surface Lagrangian current estimates from HF radars. In section 5, further improvements on the spectra reconstruction methodology and recommendations for wave–current interaction models are provided. Conclusions are summarized in section 6.

2. Methodology

WW3 is a third-generation spectral wave model (Tolman 2009; Chawla et al. 2013) providing global and regional wave hindcasts and forecasts. The model results are archived in three different formats: (i) complete directional wave spectra $S_{\eta\eta}(f, \theta)$ at limited grid points, usually coinciding with NDBC buoy locations; (ii) bulk wave parameters (H_s, T_p, θ_m, at each grid point) without any directional spread σ_θ information; and (iii) partitioned bulk wave parameters at each grid point. The latter output consists of bulk H_s, T_p, θ_m, and σ_θ values for areas of $S_{\eta\eta}(f, \theta)$ around local spectral peaks (i.e., spectral partitions). Further description on WW3 spectral partitioning is provided elsewhere (Vincent and Soille 1991; Hanson and Phillips 2001; Hanson and Jensen 2004; Tracy et al. 2007).

Here, directional wave spectra $S_{\eta\eta}(f, \theta)$ are reconstructed individually for each set of bulk partition parameters (to be combined later). First, a JONSWAP frequency spectrum $S_{\eta\eta}(f)$ (Hasselmann et al. 1973) is generated from the partition's H_s and T_p values. The selection of the peak enhancement factor γ for the JONSWAP spectrum is arbitrary, although a best fit to WW3 modeled $S_{\eta\eta}(f)$ at a nearby offshore buoy location

TABLE 1. Example of partitioned bulk parameters used for the reconstruction of a complete directional spectra.

Partition No.	H_s (m)	T_p (s)	θ_m (°)	σ_m (°)
1	2.58	6.91	304.2	22.71
2	1.01	15.82	188.5	12.18
3	0.5	19.52	90	6.54

can be used. Subsequently, frequency-invariant directional characteristics are assigned (Mitsuyasu et al. 1975):

$$D(\theta) = \frac{2^{2s-1}}{\pi} \frac{\Gamma(s+1)^2}{\Gamma(2s+1)} \cos^{2s} \frac{(\theta - \theta_m)}{2}, \quad (1)$$

where θ_m is the mean direction of the particular partition, Γ is the gamma function, and s is related to the partition's directional spread σ_θ (Kuik et al. 1988) by

$$s = \frac{2}{\sigma_\theta^2} - 1. \quad (2)$$

The directional distribution is defined so that

$$\int_0^{2\pi} D(\theta)\, d\theta = 1. \quad (3)$$

Frequency-dependent direction and directional spread are considered later (section 5a). The directional spectra for each partition are

$$S_{\eta\eta}(f, \theta) = S_{\eta\eta}(f) D(\theta). \quad (4)$$

The complete $S_{\eta\eta}(f, \theta)$ is constructed using the individual partition-based spectra [see Eq. (4)] as

$$S_{\eta\eta}(f, \theta) = \sum_{i=1}^{i=N} S_{\eta\eta}^{(i)}(f, \theta), \quad (5)$$

where N is the total number of partitions. This estimate is hereinafter referred to as the partition-based spectra and labeled as pWW3.

Instead of using individual partitions as described above, the nonpartitioned bulk wave parameters can be used to reconstruct $S_{\eta\eta}(f, \theta)$; this estimate will be referred to as nonpartition-based spectra and labeled as bWW3. The implications of using this procedure as well as a comparison of the different spectra are presented and discussed in sections 3 to 5.

An example of the reconstruction process outlined earlier is presented here using the WW3 partitioned wave parameters product for the grid point corresponding to the NOAA/NDBC Diamond Shoals buoy (DS; station ID 41025; http://www.ndbc.noaa.gov/station_history.php\?station=41025). The spectrum consists of three partitions (see Table 1) with energy in the wind

band (partition 1) and swell bands (partitions 2 and 3). The JONSWAP frequency spectrum $S_{\eta\eta}(f)$ for each individual partition is shown in Figs. 1a$_1$–1a$_3$. The corresponding directional distribution $D(\theta)$ for each partition is estimated from Eq. (1), and the frequency-integrated directional spectrum [$S_{\eta\eta}(\theta)$; Eq. (B.1)] for each partition is shown in Figs. 1b$_1$–1b$_3$. The individual partition spectra (Figs. 1c$_1$–1c$_3$) are added together to create the full directional wave spectrum $S_{\eta\eta}(f, \theta)$ [Fig. 1c$_4$; Eq. (5)].

a. Application of spectrum reconstruction method

Reconstructed partition-based spectra $S_{\eta\eta}(f, \theta)$ are compared to WW3-simulated full $S_{\eta\eta}(f, \theta)$ at NOAA/NDBC buoys Harvest (Station ID 46218; http://www.ndbc.noaa.gov/station_page.php?station=46218) located in the SCB (Figs. 2a,b) and Diamond Shoals in the Mid-Atlantic Bight (Fig. 2c). For both the locations a peak enhancement factor of $\gamma = 2$ is used for reconstruction. This choice of γ is from best-fit to WW3-modeled $S_{\eta\eta}(f)$ at the Harvest buoy (HB) for January 2006 and Diamond Shoals buoy for February 2006. Even though $\gamma = 2$ works for both locations, with primarily swell activity on the west coast (O'Reilly et al. 2016; Crosby et al. 2016) and predominantly wind-generated waves on the east coast, the choice of γ requires more thought and is further discussed in sections 2b and 5a.

The reconstructed $S_{\eta\eta}(f, \theta)$ at the Harvest buoy location consists of two swell band partitions (Fig. 2a$_2$) and compares well to WW3-simulated $S_{\eta\eta}(f, \theta)$ (Fig. 2a$_1$). The difference in total energy density $\iint S_{\eta\eta}(f, \theta)\, df\, d\theta$ from reconstructed and WW3-simulated $S_{\eta\eta}(f, \theta)$ is negligible, and therefore to identify the difference in shape of the frequency $S_{\eta\eta}(f)$ and directional spectra $S_{\eta\eta}(\theta)$, normalized frequency $S_{\eta\eta}(f)df/\int S_{\eta\eta}(f)\, df$ and directional $S_{\eta\eta}(\theta)d\theta/\int S_{\eta\eta}(\theta)\, d\theta$ spectra are compared (e.g., Fig. 2a$_3$–2a$_4$). Reconstructed and WW3-simulated $S_{\eta\eta}(f)df/\int S_{\eta\eta}(f)\, df$ (see red and black lines, respectively, Fig. 2a$_3$) have similar frequency variability; however, the reconstructed $S_{\eta\eta}(f, \theta)$ slightly underestimates the peak energy. Normalized directional spectra $S_{\eta\eta}(\theta)d\theta/\int S_{\eta\eta}(\theta)\, d\theta$ also agree well (Fig. 2a$_4$). Nonpartitioned bulk wave parameters are also used to reconstruct the spectrum. In this case, $S_{\eta\eta}(f)df/\int S_{\eta\eta}(f)\, df$ and $S_{\eta\eta}(\theta)d\theta/\int S_{\eta\eta}(\theta)\, d\theta$ (gray dots; Figs. 2a$_3$–2a$_4$) favorably compare to partition-based reconstructed and WW3-simulated normalized spectra.

The second example (Figs. 2b$_1$–2b$_4$), from Harvest buoy (data for 0000 UTC 19 June 2006) shows a reconstructed partition-based $S_{\eta\eta}(f, \theta)$ (Fig. 2b$_2$) that consists of three partitions, all in the swell band, but with different directions. The reconstructed spectrum is very similar to that produced by WW3 (Fig. 2b$_1$). The normalized
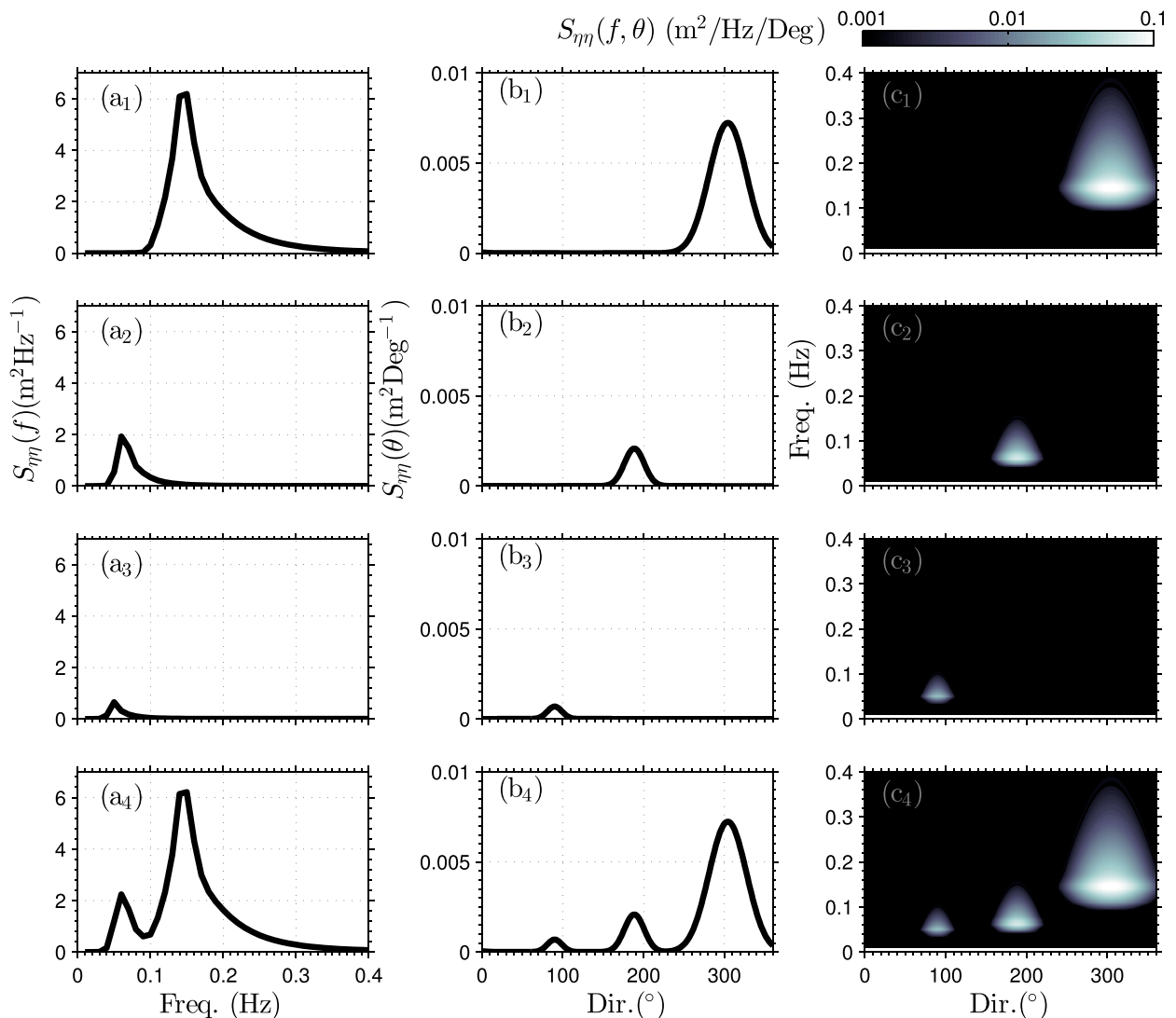
FIG. 1. (a_1)–(a_4) Frequency $S_{\eta\eta}(f)$ (m^2 Hz^{-1}), (b_1)–(b_4) directional $S_{\eta\eta}(\theta)$ (m^2 deg^{-1}), and (c_1)–(c_4) frequency directional $S_{\eta\eta}(f, \theta)$ (m^2 Hz^{-1} deg^{-1}) energy density spectra for partitions (first row) 1, (second row) 2, (third row) 3, and (fourth row) the complete reconstructed spectrum. Details of the bulk wave parameters used to create individual partitions are provided in Table 1.

spectra $S_{\eta\eta}(f)df / \int S_{\eta\eta}(f)\,df$ and $S_{\eta\eta}(\theta)d\theta / \int S_{\eta\eta}(\theta)\,d\theta$ in this case also agree well (cf. red and black lines; Figs. 2b$_3$–2b$_4$). The nonpartition-based $S_{\eta\eta}(f, \theta)$ discrepancies in $S_f df / \int S_f\,df$ and $S_d d\theta / \int S_d\,d\theta$ are apparent (see gray dots in Figs. 2b$_3$–2b$_4$).

Finally, an example representing a multimodal, multidirectional reconstructed and WW3-simulated $S_{\eta\eta}(f, \theta)$ is shown in Figs. 2c$_1$–2c$_2$ representing data from the Diamond Shoals buoy location (2100 UTC 25 February 2010). In this example, wave energy at both the swell and wind-sea frequency bands are present with different directions each. Even in this complex case, the partition-based $S_{\eta\eta}(f, \theta)$, $S_{\eta\eta}(f)df / \int S_{\eta\eta}(f)\,df$, and $S_{\eta\eta}(\theta)d\theta / \int S_{\eta\eta}(\theta)\,d\theta$ favorably compare to WW3-simulated spectra (see red and black

lines in Figs. 2c$_3$–2c$_4$), while the nonpartition-based spectrum compares poorly to the WW3 full spectral estimate (see gray dots in Figs. 2c$_3$–2c$_4$).

b. Reconstruction algorithm limitations

As shown in Fig. 2, the partition-based reconstruction algorithm [see Eqs. (1)–(5)] is capable of estimating accurate $S_{\eta\eta}(f, \theta)$ for multiple wave condition scenarios. However, for certain conditions the algorithm's performance might be limited. These specific cases are presented here (see Fig. 3) and are taken from examples for the West and East Coast of the United States: two environments with different wave patterns. Like section 2a, a constant peak enhancement factor $\gamma = 2$ is used.
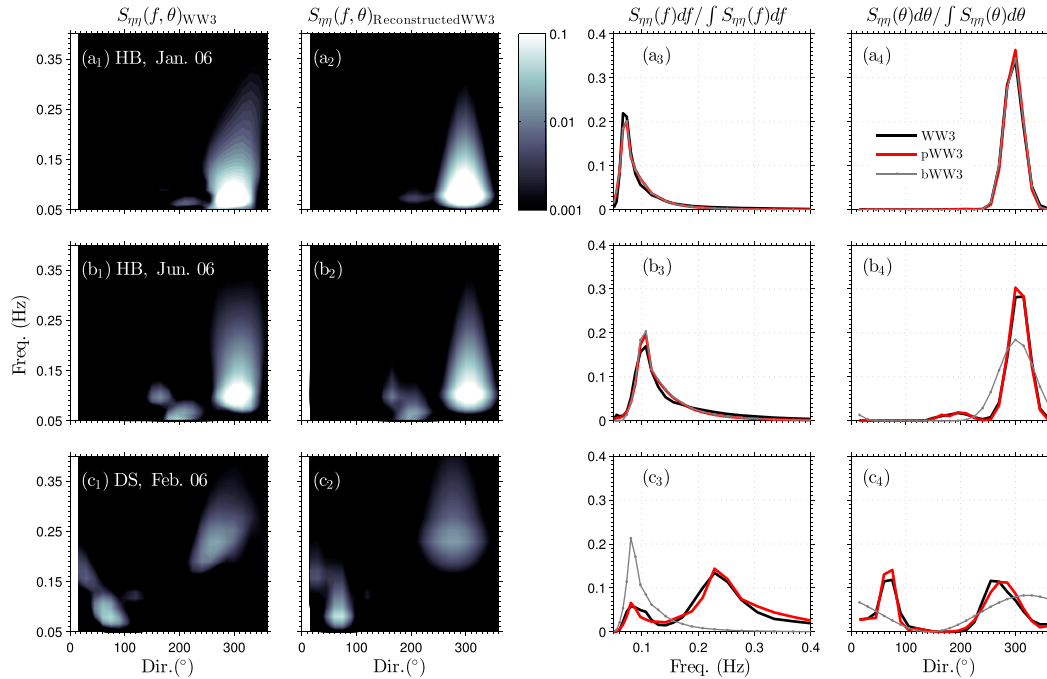
FIG. 2. (a$_1$),(b$_1$),(c$_1$) WW3-simulated vs (a$_2$),(b$_2$),(c$_2$) reconstructed $S_{\eta\eta}(f, \theta)$ at Harvest buoy (NDBC ID 46218) in the Southern California Bight at 0600 UTC 20 Jan 2006 in (a$_1$) and (a$_2$) and 0000 UTC 16 Jun 2006 in (b$_1$) and (b$_2$) and at the Diamond Shoals buoy (NDBC ID: 41025) in the Mid-Atlantic Bight at 2100 UTC 25 Feb 2010 in (c$_1$) and (c$_2$). (a$_3$),(b$_3$),(c$_3$) Normalized frequency $S_{\eta\eta}(f)df/\int S_{\eta\eta}(f)\,df$ and (a$_4$),(b$_4$),(c$_4$) directional $S_{\eta\eta}(\theta)d\theta/\int S_{\eta\eta}(\theta)\,d\theta$ spectra from reconstructed (partitioned bulk parameters in red; nonpartitioned bulk parameters in gray) and simulated WW3 (black) spectrum.

In the first example (Fig. 3a$_1$), a WW3-simulated $S_{\eta\eta}(f, \theta)$ at the Harvest buoy (1200 UTC 2 January 2006) is shown; it has multiple peaks, and it is characterized by a directional asymmetry that occurs mainly during periods of rapidly shifting wind direction (e.g., Wang and Hwang 2001). The partition-based $S_{\eta\eta}(f, \theta)$ (Fig. 3a$_2$) has similar distribution to WW3-simulated $S_{\eta\eta}(f, \theta)$; however, it does not reproduce the asymmetric behavior at higher frequencies (Fig. 3a$_2$). Discrepancies are evident in $S_{\eta\eta}(f)df/\int S_{\eta\eta}(f)\,df$ and $S_{\eta\eta}(\theta)d\theta/\int S_{\eta\eta}(\theta)\,d\theta$ (Figs. 3a$_3$–3a$_4$) as well. In particular, the reconstructed $S_{\eta\eta}(f)df/\int S_{\eta\eta}(f)\,df$ (red Fig. 3a$_3$) overestimates energy at the peak frequency and consequently underestimates at lower and higher frequencies. This discrepancy indicates that the peak enhancement factor $\gamma = 2$ selected in this case based on the best fit for Harvest buoy, June 2006, is not suitable. Also, the reconstructed $S_{\eta\eta}(\theta)d\theta/\int S_{\eta\eta}(\theta)\,d\theta$ is broader and does not compare favorably to WW3-simulated $S_{\eta\eta}(\theta)d\theta/\int S_{\eta\eta}(\theta)\,d\theta$.

At Diamond Shoals (Fig. 3b) the reconstructed and WW3-simulated $S_{\eta\eta}(f, \theta)$ (for 0900 UTC 6 February 2010) are similar for f less than 0.15 Hz. However, at higher frequencies the algorithm does not create the asymmetric directional distribution (Figs. 3b$_1$–3b$_2$).

The $S_{\eta\eta}(f)df/\int S_{\eta\eta}(f)\,df$ do not agree well for $0.15 < f < 0.20$ Hz (Fig. 3b$_3$). The reconstruction-based $S_{\eta\eta}(\theta)d\theta/\int S_{\eta\eta}(\theta)\,d\theta$ is symmetric with respect to θ and rolls off faster than the WW3-based $S_{\eta\eta}(\theta)d\theta/\int S_{\eta\eta}(\theta)\,d\theta$ (Fig. 3b$_4$).

In summary, the reconstructed $S_{\eta\eta}(f, \theta)$ is most accurate when WW3-simulated spectra satisfy the assumptions about the choice of peak enhancement factor γ and directional symmetry [Eq. (1)]. Reconstructions of skewed (in frequency or direction) energy distributions are less accurate and would benefit from improved γ estimation by using the peak spectral energy of the partition and additional bulk parameters like mean period T_m, peak energy direction θ_p, directional spread σ_p at peak period, and zero-up-crossing wave period T_z at the peak period, which describe higher-order details of the spectra. Improvements in $S_{\eta\eta}(f, \theta)$ reconstruction by using these additional parameters are suggested in section 5a.

3. Application in numerical modeling

a. Model setup

Here, we evaluate the skill of the reconstruction methodology (section 2a) to parameterize the offshore
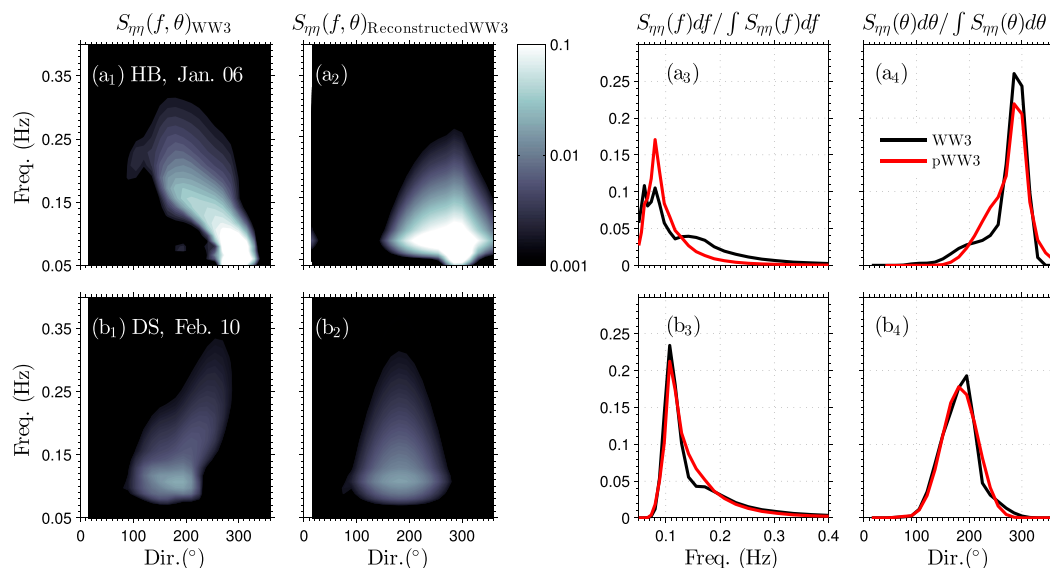
FIG. 3. (a$_1$),(b$_1$) WW3-simulated vs (a$_2$),(b$_2$) reconstructed $S_{\eta\eta}(f,\theta)$ at HB (NDBC ID 46218) in the Southern California Bight at 1200 UTC 2 Jan 2006 in (a$_1$) and (a$_2$) and DS (NDBC ID 41025) in Mid-Atlantic Bight at 0900 UTC 6 Feb 2010 (b$_1$) and (b$_2$). (a$_3$),(b$_3$) Normalized frequency $S_{\eta\eta}(f)df/\int S_{\eta\eta}(f)\,df$ and (a$_4$),(b$_4$) directional $S_{\eta\eta}(\theta)d\theta/\int S_{\eta\eta}(\theta)\,d\theta$ spectra from reconstructed (red) and WW3 simulated (black) are also shown.

regional wave model boundary condition in simulations for the SCB. The SCB is located on the U.S. West Coast extending from the United States/Mexico border (32.5°N) to Point Conception (34.6°N) and is characterized by complicated bathymetry, including a number of offshore islands, shallow banks, and submarine canyons (Fig. 4). The regional geomorphology modifies surface gravity wave propagation and shelters the nearshore (e.g., Pawka et al. 1984). The SCB wave climatology is consequently spatially complex owing to depth-limited shoaling, refraction, diffraction (e.g., O'Reilly and Guza 1991, 1993), and has been well studied (e.g., Rogers et al. 2007; Barnard et al. 2014; O'Reilly et al. 2016; Crosby et al. 2016).

Waves are simulated with the spectral wave generation and propagation model Simulating Waves Nearshore (SWAN; Booij et al. 1999; Ris et al. 1999). The model grid has a resolution $\Delta X = \Delta Y = 500\,\text{m}$ with 801×421 grid points. Wind forcing is provided from the North American Regional Reanalysis (NARR) model with a resolution of 32 km. At the offshore open boundaries (north, west, and south), wave information is provided from WW3 hindcast using two different approaches. In the first case (run A), a time series of along-boundary, varying, nonpartitioned, bulk wave parameters H_s, T_p, and θ) is used. As the WW3 hindcast in this bulk wave parameter format does not provide any directional spread information, regional wave model simulations are either forced with an arbitrarily chosen σ_θ (e.g., Hopkins et al. 2016) or information regarding σ_θ is not detailed (e.g., Olabarrieta et al. 2012). Here, a constant $\sigma_\theta = 20°$ is used

based on average σ_θ from the Harvest buoy for the simulation period. The model uses this information internally to create a JONSWAP spectrum with a peak enhancement factor $\gamma = 2$ for consistency and a directional distribution identical to that of Eq. (1). In the second case (run B), time series of WW3 partitioned wave information are used to reconstruct the full spectra along all open boundaries using the approach discussed in section 2a. Model simulations for each run are conducted for a period of 1 month: 1–30 June 2006. The SWAN
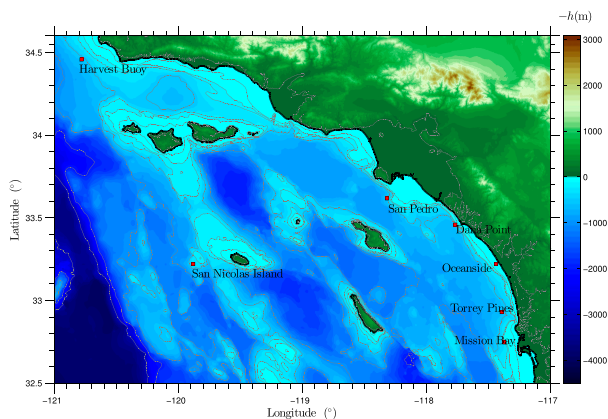

FIG. 4. Model domain used for simulating waves in the Southern California Bight. The color shading represents bathymetry, while red squares show the location of offshore NOAA buoy locations used for model verification and comparison of reconstructed and simulated spectra (see text for details).

wave action balance equation is solved in frequency and directional space with 48 frequencies between 0.0 and 1.00 Hz and 60 directional bands with a directional width of 6°. The ratio of wave height to water depth at which wave breaking occurs is set to 0.5.

b. Model data comparison at buoy locations

Modeled and observed H_s, T_m, θ_m, and σ_θ are compared at two locations:[1] San Nicolas Island buoy and the Oceanside buoy (see Fig. 4).

At the San Nicolas Island (Fig. 5), observed H_s varies from 1 to 3.5 m. Significant wave heights greater than 3 m are observed on days 165–168 and 170–172 (Fig. 5a). Mean wave period T_m varies between 5 and 12 s (Fig. 5b), while the mean direction θ_m is usually from 300° to 360°N (Fig. 5c). Directional spread values vary from 20° to 40° (Fig. 5d). Simulations conducted using the partition-based directional spectra $S_{\eta\eta}(f, \theta)$ (run B, red lines in Fig. 5) favorably compare to observations of H_s, T_m, θ_m, and σ_θ (red lines in Figs. 5a–d). However, the simulations with bulk wave parameter boundary conditions (i.e., internally generated, nonpartitioned spectrum; run A) overestimate H_s, especially during days 151–154, 156–159, and 175–180 (gray lines; Fig. 5a). Mean wave period (Fig. 5b) is also overestimated for a number of 5-day periods. The mean direction θ_m favorably compares to observations (gray line; Fig. 5c). The change in the wave direction from $\theta_m = 300°$ to 200° occurs due to a south swell event (e.g., Adams et al. 2008). The directional spread is either under- or overestimated throughout the model simulation period (Fig. 5d). Root-mean-square (rms) error estimates for these comparisons are listed in Table 2.

At the Oceanside buoy (Fig. 4), observed H_s (see black line; Fig. 5a) reaches values up to 1.5 m, while the corresponding T_m values range from 5 to 10 s (Fig. 5b). Wave mean direction θ_m is usually between 0° and 100°, while the σ_θ values range from 30° to 40° (Figs. 5c,d). The H_s estimates from the partition-based reconstructed $S_{\eta\eta}(f, \theta)$ (see red lines in Fig. 5a) compare favorably to buoy observations. Modeled and observed T_m and θ_m values are similar to each other (see red and black lines in Figs. 5b,c), while the modeled directional spread (red,

line in Fig. 5d) is slightly lower for the entire simulation period. The H_s estimates from run A (i.e., nonpartition-based spectral boundary conditions; see gray lines in Fig. 5a) are higher than measured values during days 150–165, while T_m is higher for the entire simulation period (Fig. 5b). Mean wave direction θ_m (Fig. 5c) compares favorably, while σ_θ is underestimated (Fig. 5d).

Overall, at both locations (i.e., San Nicolas Island and Oceanside), model results with partition-based $S_{\eta\eta}(f, \theta)$ compare favorably against the in situ buoy observations, reducing the rms error between simulation and measurements by 50% for H_s and even more for the other wave parameters, especially in the San Nicholas location (see Table 2). Only at the Oceanside location the improvement for θ_m and σ_θ is ≈10%. Similar agreement with data and simulation results are found at other buoy locations, for example, San Pedro, Dana Point, Torrey Pines, and Mission Bay (not shown here).

c. Effects on wave climatology estimations

Monthly mean H_s for June 2006, within the SCB, are estimated using runs A and B (see Figs. 6a and 6b, respectively). These are compared to the WW3 hindcast (U.S. West Coast, grid 2, 1/25°) monthly mean H_s that is shown in Fig. 6c. In general, increased geographic resolution (e.g., 500 m) is preferred in the Southern California Bight to better represent the wave energy blocking from the islands within the bight and also focus, defocusing, shoaling, and dissipation of energy (e.g., Rogers et al. 2007). Here, the WW3 hindcast is substantially coarser (≈4.4 km) than those for SWAN simulations. Nonetheless, SCB is highly sensitive to the blocking of wave energy from some directions (Rogers et al. 2007; Crosby et al. 2016), and implications for using nonpartitioned versus partitioned spectral information can still be delineated through comparison to coarse WW3 hindcast.

Partitioned spectral forcing simulations produced monthly mean values of H_s less than 1 m in the areas east of the Santa Barbara Channel (SBC), within the San Pedro Basin (SPB), and adjacent to the coast from Oceanside to Mission Bay (Fig. 6b). The effect of offshore island shadowing is strong in the SPB and in the region onshore, off San Nicolas Island. In the shelf region of the SCB (water depth $h > 50$ m), H_s varies from 1 to 1.5 m. In contrast, the results from run A indicate monthly mean H_s values varying from 0 to 3 m, with relatively higher values in the interior region of the bight (Fig. 6a). In the SPB, mean H_s varies between 1 and 1.5 m, and the relative effect of wave shadowing through offshore islands is significantly reduced (Fig. 6b).

Comparing monthly mean H_s values estimated from the WW3 hindcasts (Fig. 6c), we find a very good

---

[1] A directional wave buoy only estimates the first five Fourier coefficients a_0, a_1, b_1, a_2, and b_2 (Longuet-Higgins et al. 1961), which do not determine the complete directional spectrum and therefore cannot be used to estimate θ_m and σ_θ as in Eqs. (B.4) and (B.5). Instead, θ_1, θ_2, σ_1, and σ_2 can be estimated from the Fourier coefficients following Kuik et al. (1988) and Herbers et al. (1999). Here, for brevity modeled and directional buoy-based θ_2 and σ_2 are compared, and for simplicity are referred to as θ_m and σ_θ in the rest of the manuscript. The findings from comparison between observed and modeled θ_1 and σ_1 are similar and not shown here.
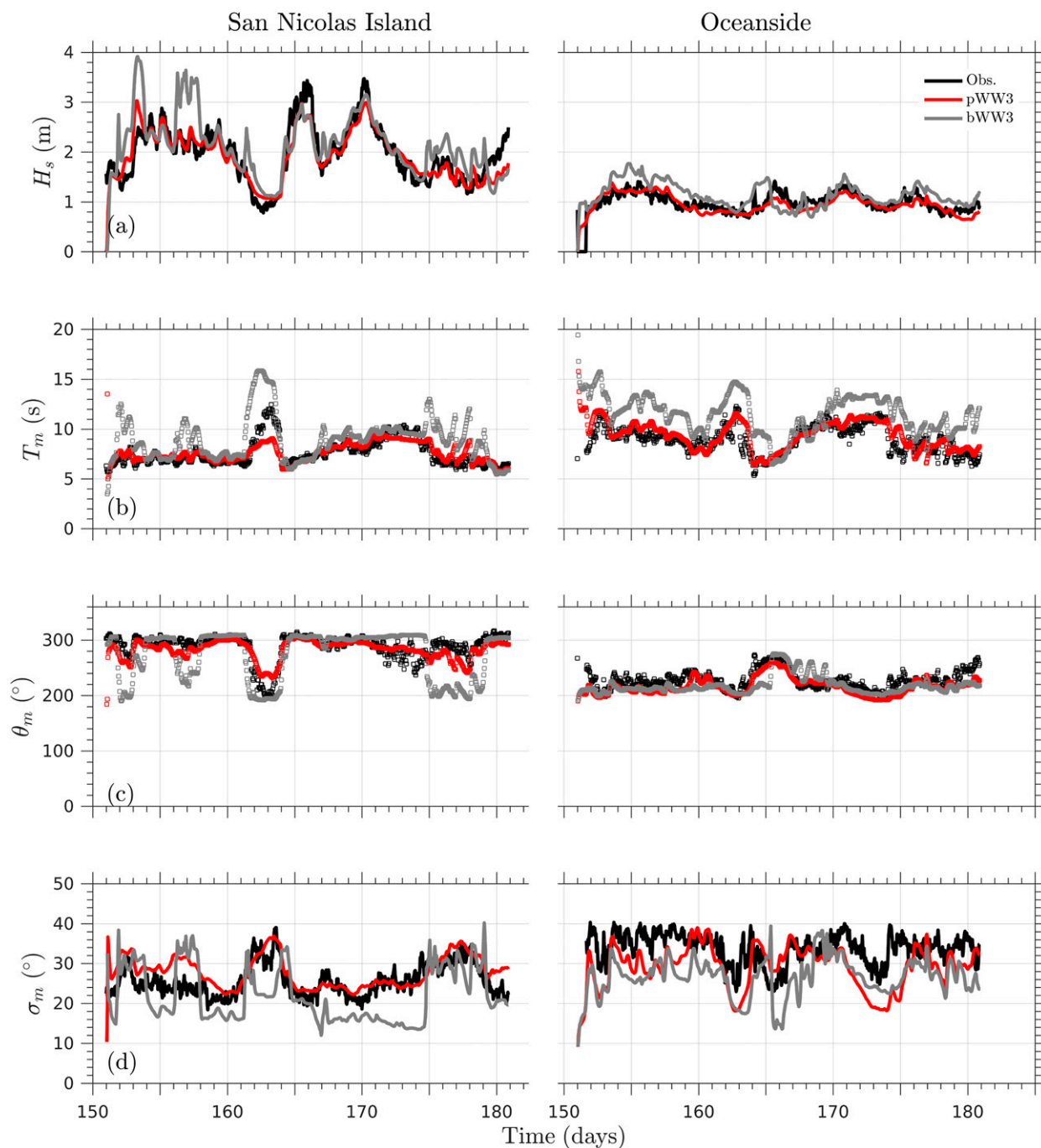
FIG. 5. Comparison of observed (black) and simulated wave parameters using simulations with reconstructed spectra (red, pWW3) and bulk wave parameters (gray, bWW3) as boundary conditions. (a) Significant wave height H_s, (b) mean wave period T_p, (c) mean wave direction θ_m, and (d) directional spreading σ_m vs time at (left) San Nicolas Island and (right) Oceanside.

agreement with the values estimated using the results of the partition-based spectral boundary condition (run B). The comparison is favorable in the offshore region of SCB (i.e., $h > 500$ m; see Fig. 6), but also the wave-sheltering effects in SPB and onshore of San Nicolas island are similar. On the contrary, H_s estimates from

the run with the nonpartition-based spectra boundary conditions (run A) are substantially higher especially in water depths greater than 500 m. These discrepancies are expected to be similar for other bulk wave parameters within the SCB, which will affect Stokes drift and wave-driven circulation estimates.

TABLE 2. Root-mean-square error estimates for bulk wave parameters at two SCB buoys (for location see Fig. 4) estimated using the reconstructed spectra (pWW3) as boundary conditions and using the bulk wave parameters (bWW3).

	H_s (m)	T_m (s)	θ_m (°)	σ_m (°)
San Nicolas Island				
pWW3 (1)	0.25	0.80	22.48	3.61
bWW3 (2)	0.51	2.14	63.96	7.36
Ratio (1)/(2)	0.49	0.37	0.35	0.49
Oceanside				
pWW3 (1)	0.14	0.96	30.63	6.73
bWW3 (2)	0.27	2.91	33.83	8.34
Ratio (1)/(2)	0.52	0.33	0.90	0.81

4. Implications for HF radar surface current estimates

a. HF radar current measurements

High-frequency radars estimate surface ocean currents by analyzing the Doppler shift in the Bragg scattered return signal (Crombie 1955). The ocean Bragg wave phase speed deviates from linear wave theory due to a combination of surface Eulerian mean current and the surface gravity wave field (Barrick and Weber 1977). The traditional approach of subtracting the linear wave theory phase speed (e.g., Paduan and Washburn 2013) results in a surface current measurement that is neither truly Eulerian nor Lagrangian (e.g., Ardhuin et al. 2009). Following Barrick and Weber (1977), the phase speed c_b measured by HF radar is

$$c_b = c_0 + u^r, \tag{6}$$

where c_0 is the linear wave theory phase speed, and u^r is the radial surface current measurement. The latter can be written as follows:

$$u^r = \mathbf{u}^E \cdot \hat{\mathbf{r}} + u_f^{St}, \tag{7}$$

where $\mathbf{u}^E$ is the Eulerian mean current, and $\hat{\mathbf{r}}$ is a unit vector in the radar look direction; u_f^{St}, the filtered Stokes drift, is a function of the surface wave field and the radar site characteristics (Barrick and Weber 1977; Broche et al. 1983; Ardhuin et al. 2009). The true Lagrangian current u^L in the radar look direction is defined as

$$\begin{aligned} u^L \cdot \hat{\mathbf{r}} &= \mathbf{u}^E \cdot \hat{\mathbf{r}} + \mathbf{u}^{St} \cdot \hat{\mathbf{r}} \\ &= u^r - u_f^{St} + \mathbf{u}^{St} \cdot \hat{\mathbf{r}}, \end{aligned} \tag{8}$$

where $\mathbf{u}^{St}$ is the Stokes drift vector. The last two terms in Eq. (8) define the not measured (i.e., missing) part of the Stokes drift along the radar look direction defined as

$$u_{er}^r = \mathbf{u}^{St} \cdot \hat{\mathbf{r}} - u_f^{St}, \tag{9}$$
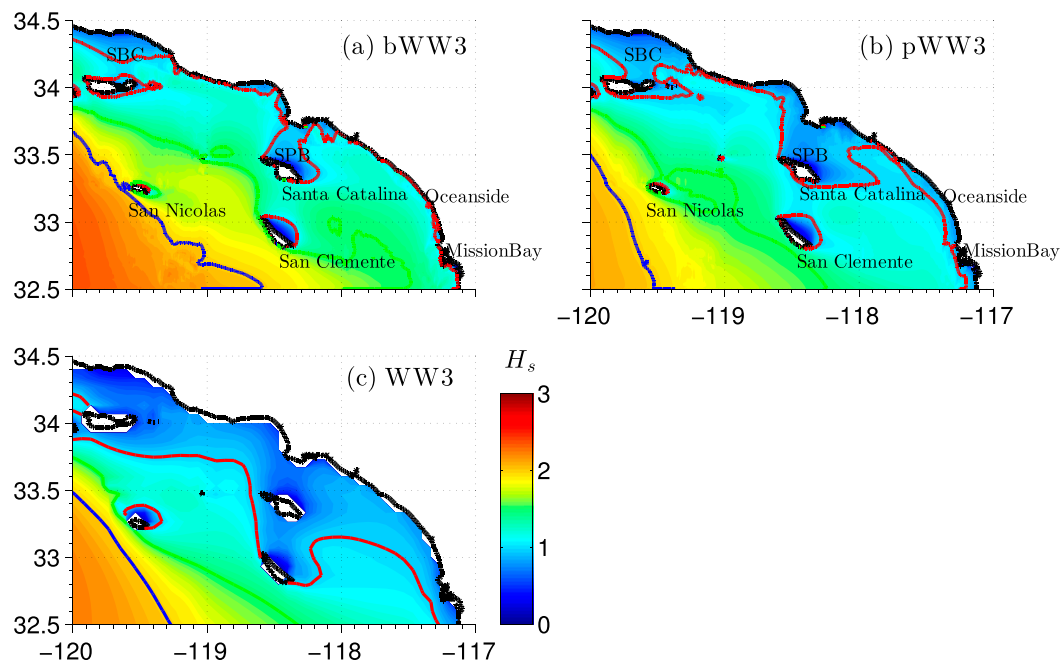

FIG. 6. Mean significant wave height H_s within the Southern California Bight for the month of June 2006 estimated using (a) regional model with bulk wave parameter as boundary conditions, (b) regional model with spectral wave boundary conditions, and (c) global WW3. Only a part of the modeling domain is shown in this figure. The thick black line is the bathymetric zero contour line, while the thin gray line is $h = 500$ m. The red, green, and blue lines correspond to 1.0-, 1.5-, and 2.0-m wave height contours, respectively.
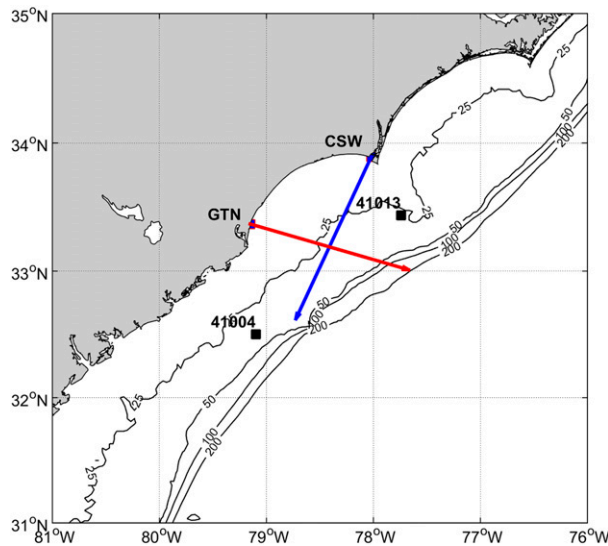
FIG. 7. Region of South Atlantic Bight covered by HF radars located at GTN and CSW. The line of site from GTN and CSW are the red and blue vectors, respectively. The intersection point is the position from which the measured currents are shown in Fig. 8. The water depth at this measurement point is 27 m. Solid black lines are 25-, 50-, 100-, and 200-m isobaths. Black squares indicate the locations of NDBC buoys (IDs 41013 and 41804). Each radar site measures the surface current velocity projected along the line of site (i.e., radial velocity).

which can introduce error into HF radar–based surface Lagrangian trajectory estimates.

Stokes drift estimates from a wave propagation numerical model can be used to carry out such corrections (Cahl and Voulgaris 2016). Estimation of u_f^{St} and $\mathbf{u}^{St}$ requires knowledge of the full directional wave spectrum (Barrick and Weber 1977; Broche et al. 1983; Ardhuin et al. 2009). The sensitivity of the correction u_{er}^r on the type of reconstructed directional wave spectrum (i.e., partition versus nonpartition based) is examined in the next section.

b. HF radar Lagrangian calculations

HF radar surface current measurements and concurrent WW3 partitioned and total bulk wave parameters were acquired for January 2013 at 33.2°N, 78.4°W in Long Bay, South Carolina. This area is covered by two HF radar sites located at Georgetown, South Carolina (GTN), and Fort Caswell, North Carolina (CSW), respectively (see Fig. 7). This configuration has a range resolution of 3 km, and surface current is estimated on a 3-km orthogonal grid by beam forming the radar signal at the each grid point. Wave generation in Long Bay, South Carolina, is mostly wind driven (Wu et al. 2017, manuscript submitted to *Ocean Dyn.*). Low-pass filtered winds (from NOAA/NDBC station ID 41013) and H_s presented as a directional vector are shown in Fig. 8. The missing Stokes drift u_{er}^r estimates with

$\mathbf{u}^{St}$ [Eq. (A.1a)] and u_f^{St} from partition- and nonpartition-based $S_{\eta\eta}(f, \theta)$ are considered for the radial velocities from each radar site (GTN and CSW; see Figs. 8c,d). The mean wave direction θ_m closely follows the wind direction (Figs. 8a,b). Large swell trains that can significantly bias nonpartition-based $S_{\eta\eta}(f, \theta)$ reconstruction (e.g., Fig. 2c₄) are not present in this region. Nonetheless, the u_{er}^r differences from nonpartition- and partition-based reconstructions are significant when multiple partitions are present (Figs. 8c,d). For example, CSW u_{er}^r estimates on day 14, derived using nonpartition-based spectra, is the inverse of those from partition-based spectra reconstructions (Fig. 8d). These differences are up to $5\,\mathrm{cm\,s^{-1}}$ and similar to differences observed between ADCP and HF radar measurements (Liu et al. 2014) but also between drifter and HF radar measurements (Rypina et al. 2014).

Although small, this error term of up to $\approx 5\,\mathrm{cm\,s^{-1}}$ could result in trajectory deviations of up to $4\,\mathrm{km\,day^{-1}}$, assuming constant wave conditions. Here, Lagrangian trajectories, calculated using nonpartitioned u_b^L and partitioned u_p^L reconstructed spectra are examined over a period of 7 days (Fig. 9). These trajectories are calculated over the HF radar coverage area using a random walk Monte Carlo simulation with a resolution of 50 m (diffusion coefficient $K_h = 20\,\mathrm{m^2\,s^{-1}}$), as described in Ullman et al. (2006) with 1000 particles released at three separate starting positions (A, B, and C) marked in Fig. 9. The last position of each particle is shown as red, black, and blue dots in Fig. 9 for u_p^L, u_b^L, and u^r, respectively. The trajectories of the center of mass of each estimate are shown as solid lines. Over a week, the separation of the center of mass between the u_p^L- and u^r-based trajectories is $\approx 10\,\mathrm{km}$, while the difference between u_b^L- and u^r-based trajectories is 3 to 8 km (Fig. 9b). This length scale of 10 km is of the same order as the submesoscale eddy length scale and demonstrates that the drifter cloud may be subjected to different eddy activity when partition-based Lagrangian velocities are used.

5. Discussion

a. Directional spectrum reconstruction algorithm refinement

Though the partition-based algorithm reconstructs wave spectra generated by WW3 and improves model predictions (section 3b), the accuracy of this method depends on choice of γ and does not fully capture asymmetric direction distributions of wave energy. Furthermore, for regional modeling on length scales of $\approx 100\,\mathrm{km}$, $S_{\eta\eta}(f, \theta)$ may not be spatially constant, and reconstruction with a best fit to γ may be limited due to sparse buoy measurements. Here, it is demonstrated that inclusion of five more parameters for each partition
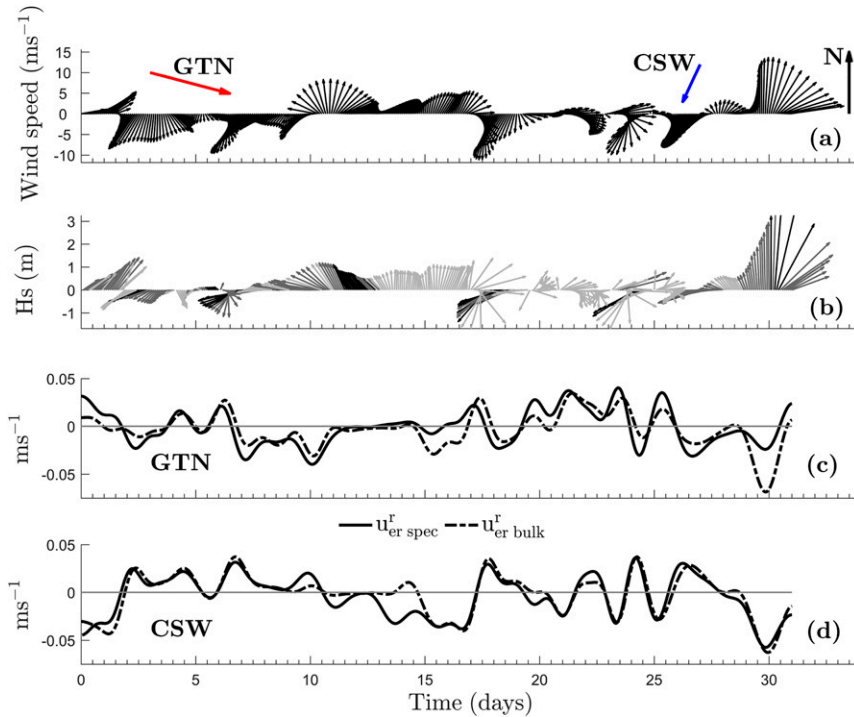
FIG. 8. (a) Time series of low-pass wind velocity vectors; the radial directions from the radar site to the measurement location for each HF radar station (GTN and CSW) are shown as red and blue arrows, respectively. (b) Time series of significant wave height H_s and direction represented as vectors from measurements from NDBC buoy 41013. Color of each vector indicates the number of partitions identified in the spectra (black = 1 partition, gray = 2 partitions, light gray = 3 or more partitions). Comparison of the differences between radial components of surface Stokes and filtered Stokes velocity u_{er}^r [Eq. (9)] estimated using bulk- (dashed) and partition-based spectral reconstruction (solid) for (c) GTN and (d) CSW, respectively.

improves the reconstruction processes (Bunney et al. 2014), including mean period T_m, peak energy direction θ_p, directional spread σ_p at the peak period, zero-up-crossing wave period T_z, and peak spectral energy $S_{\eta\eta}(f_p)$. These parameters, when available, can be used to determine, for each partition, (i) the peak enhancement factor γ and (ii) peak energy direction and directional spread variability as a function of frequency and (iii) allow the fitting of alternate spectral shapes to partitions identified as swell (if exist). Here, the first two effects are considered. For example, in order to accurately estimate the peak enhancement factor γ, first a Pierson–Moskowitz (PM) spectrum $S_{\eta\eta}(f)$ (Pierson and Moskowitz 1964) is constructed using the partitioned H_s and T_p. The JONSWAP and PM spectrum are related such that $S_{\eta\eta}(f)_{\text{JONSWAP}} = \gamma^{L(f)} S_{\eta\eta}(f)_{\text{PM}}$, where $L(f)$ is a frequency-dependent exponential function. The γ value is estimated as the ratio of the partition peak spectral energy to spectral energy of the PM spectrum at peak frequency, that is,

$$\gamma = \max\left\langle 1.0, \frac{S_{\eta\eta}(f_p)}{S_{\eta\eta}(f_p)_{\text{PM}}}\right\rangle. \qquad (10)$$

Following Bunney et al. (2014), the skewed wind-sea system can be represented using a directional spread formulation that modifies the peak direction and the directional spread as a function of frequency so that

$$\frac{\partial\theta}{\partial f} = \frac{\theta_p - \theta_m}{f_p - f_m}, \quad \text{and} \qquad (11a)$$

$$\frac{\partial\sigma}{\partial f} = \frac{\sigma_p - \sigma_m}{f_p - f_m}. \qquad (11b)$$

For each frequency band the peak direction and directional spread are estimated as

$$\theta(f) = \theta_p \frac{\partial\theta}{\partial f}(f - f_p) \quad \forall f \geq f_p$$
$$= \theta_p \quad \forall f < f_p, \qquad (12a)$$

and

$$\sigma(f) = \sigma_p \frac{\partial\sigma}{\partial f}(f - f_p) \quad \forall f \geq f_p$$
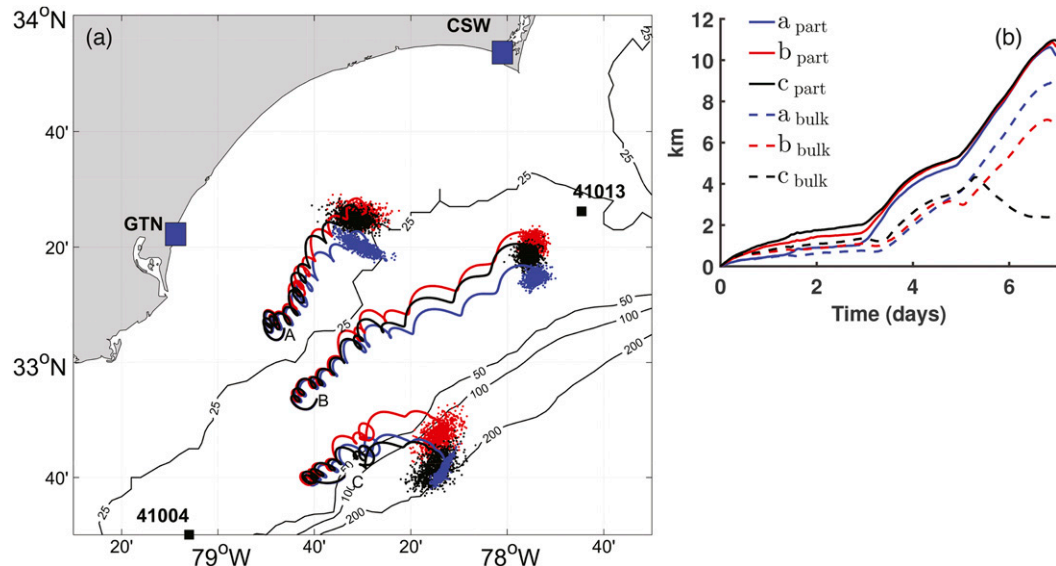$$= \sigma_p \quad \forall f < f_p \qquad (12b)$$

FIG. 9. (a) Lagrangian trajectories estimated over the period of 7 days using HF radar currents u^r (blue), Lagrangian-corrected HF radar currents using u^L_{part} (red), and u^L_{bulk} (black). Initial locations are labeled are shown as A, B, and C. (b) Separation distance of center of mass (between u^L_{part} and u^r in solid lines, between u^L_{bulk} and u^r in dashed lines) for each trajectory calculation shown in (a) with different staring points (A, B, and C).

under the assumption that directions and directional spread vary linearly with frequency.

The directional distribution $D(\theta)$ [Eq. (1)] is applied at each frequency band. The corrections suggested in Eqs. (10), (11), and (12) are applied for the two spectral reconstruction cases discussed in section 2b (see Figs. 3, 10). This reconstructed $S_{\eta\eta}(f, \theta)$ using additional parameters [i.e., Eqs. (10), (11), and (12)] is referred to as UK MET.

The reconstructed $S_{\eta\eta}(f, \theta)$ successfully recreates the asymmetry for both Harvest and Diamond Shoals buoy locations, as shown in Figs. $10a_1$–$10a_2$ and $10b_1$–$10b_2$, respectively. At the Harvest buoy, reconstructed and WW3-simulated $S_{\eta\eta}(f)df/\int S_{\eta\eta}(f)\,df$ and $S_{\eta\eta}(\theta)d\theta/\int S_{\eta\eta}(\theta)\,d\theta$ (red and black lines in Figs. $10a_3$–$10a_4$) compare favorably; however, the WW3-simulated double peak evident in $S_{\eta\eta}(f)df/\int S_{\eta\eta}(f)\,df$ is not reconstructed. At Diamond Shoals, the normalized frequency spectrum (Fig. $10b_3$) is more accurate than the original reconstruction in the frequency range 0.15–0.20 Hz.

Asymmetric directional distribution $D(\theta)$ may occur due to small-scale wind fluctuations and slant fetch effects that occur when offshore winds are oblique to the shoreline orientation leading to asymmetric fetch (Ewans 1998; Wang and Hwang 2001; Long and Resio 2007). The implications for small-scale wind fluctuations on directional asymmetry is expected to dominate in regions with strong, local, wind-generated waves, for example, South Atlantic Bight (SAB) and Mid-Atlantic Bight, unlike the Southern California Bight with limited local wind activity (Adams et al. 2008). If the reconstruction algorithm

is used for creating $S_{\eta\eta}(f, \theta)$ in shallower coastal waters, the implications for oblique wind direction to shoreline orientation and associated directional asymmetry may lead to poor $S_{\eta\eta}(f, \theta)$ reconstruction. However, it is expected that the method outlined here will be used for creating boundary conditions for regional wave models that would modify the $S_{\eta\eta}(f, \theta)$ due to local wind effects.

b. Surface Stokes drift estimates from reconstructed $S_{\eta\eta}(f, \theta)$

The reconstruction methods used in this study improve the $S_{\eta\eta}(f, \theta)$ estimates. The choice of reconstruction method and its implication in estimating the surface Stokes drift is examined in here for Edisto (http://www.ndbc.noaa.gov/station_page.php?station=41004) and Frying Pan Shoals (http://www.ndbc.noaa.gov/station_page.php?station=41013) in the SAB (Fig. 11a), and Harvest, San Nicolas Island, and San Pedro in the SCB (Fig. 11b) using data from the period January to December 2012.

The simulated, WW3, full directional spectra at these buoy locations are partitioned and all nine parameters (section 5a) are calculated. Bulk wave parameters for the full directional spectra are also calculated. Four different reconstructed $S_{\eta\eta}(f, \theta)$ are created using (i) the standard, partitioned WW3 parameters H_s, T_p, θ_m, σ_θ (partition-based spectrum pWW3); (ii) the standard, partitioned parameters and $S_{\eta\eta}(f_p)$ (pWW3 + E); (iii) all nine parameters H_s, T_p, θ_m, σ_θ and T_m, T_p, θ_p, σ_p, $S_{\eta\eta}(f_p)$, as suggested in (Bunney et al. 2014; UK MET); and (iv) the
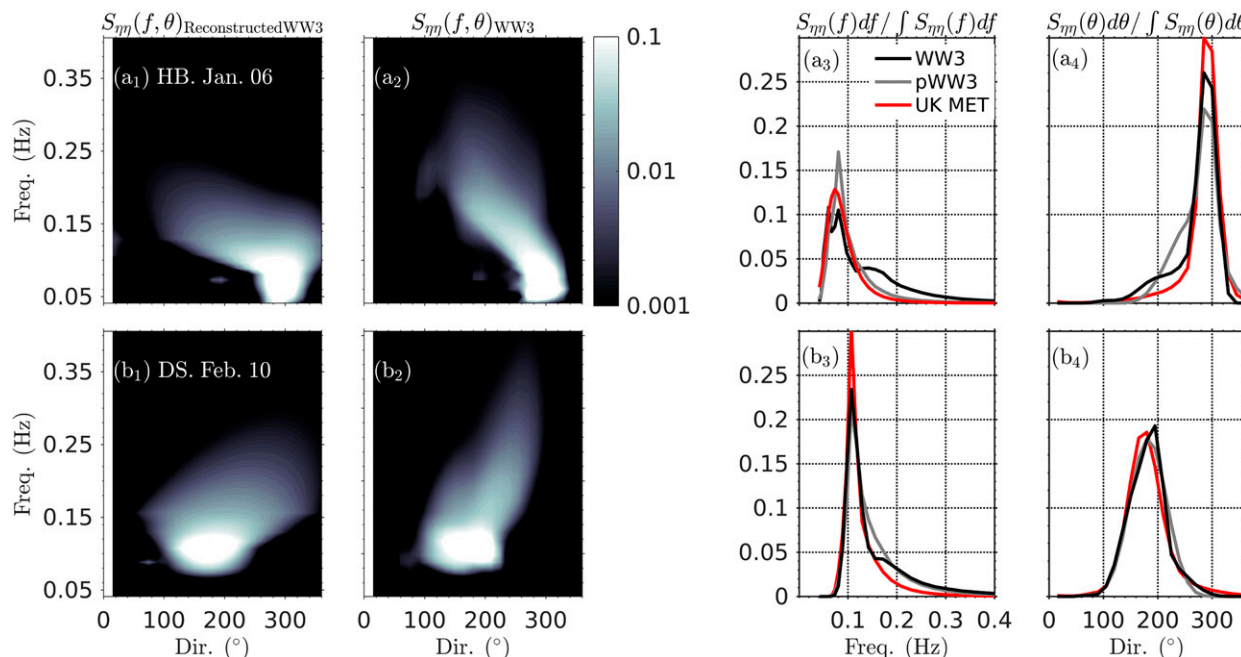
FIG. 10. $(a_1),(b_1)$ WW3-simulated and $(a_2),(b_2)$ reconstructed directional spectra using asymmetrical parameters for the HB (in SCB) at 1200 UTC 2 Jan 2006 in (a_1) and (a_2) and DS (in MAB) at 0900 UTC 6 Feb 2010 in (b_1) and (b_2). $(a_3),(b_3)$ Normalized frequency $S_{\eta\eta}(f)df/\int S_{\eta\eta}(f)\,df$ and $(a_4),(b_4)$ directional $S_{\eta\eta}(\theta)d\theta/\int S_{\eta\eta}(\theta)d\theta$ spectra from reconstructed (red) and simulated WW3 (black) spectral estimates are shown.

nonpartition-based spectrum (bWW3). Using these four reconstructed $S_{\eta\eta}(f,\theta)$, the surface Stokes drift is calculated and referred to as U_r^{St} (see appendix A). In addition, the same quantity is calculated using Eq. (A.2) with the wave parameters obtained from (v) the total, non-partitioned bulk wave parameters (referred to as b, Fig. 11),

a standard approach in the existing coupled ocean circulation and wave propagation model, and from (vi) the vector sum of individual Stokes drift estimates using Eq. (A.2) derived for each partition separately (hereinafter bp, Fig. 11). These Stokes drift estimates are compared to those from WW3-simulated spectra (hereinafter U_{Spec}^{St})
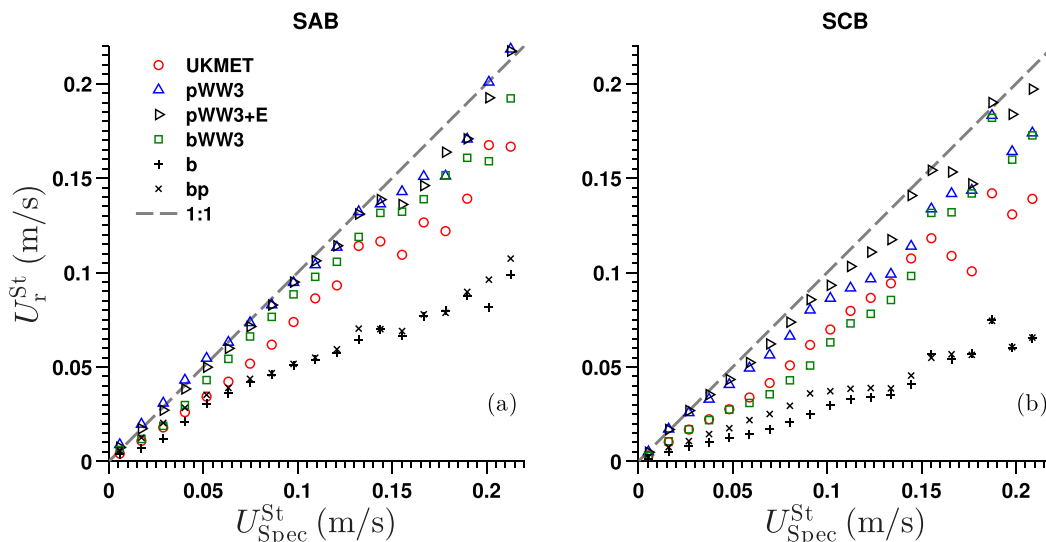

FIG. 11. Bin-averaged surface Stokes drift estimates from reconstructed spectra and bulk parameters U_r^{St} (see key legend in figure and text for details) vs Stokes drift estimates from WW3 simulated spectra U_{spec}^{St} for (a) the SAB (NDBC buoys 41004 and 41013) and (b) the SCB (NDBC buoys 46218, 46219, and 46222).

TABLE 3. Root-mean-square differences in surface Stokes velocity magnitude U and direction θ in the SAB (NOAA/NDBC buoy IDs 41013 and 41004) and the SCB (NOAA/NDBC buoy IDs 46218, 46219, and 46222) January–December 2012; m is the best-fit slope.

	pWW3	UK Met	pWW3 + E	bWW3	Eq. (A.2) Bulk	Eq. (A.2) Part.
SAB						
U (cm s^{-1})	1.5	2.1	1.2	2.17	3.4	3.0
θ (°)	15.5	21.8	15.9	33.4	33.4	27.1
m	0.98	0.73	0.95	0.86	0.51	0.55
SCB						
U (cm s^{-1})	1.9	2.3	1.5	3.0	4.4	3.9
θ (°)	10.4	17.0	10.2	24.1	24.1	23.2
m	0.83	0.67	0.92	0.61	0.27	0.36

at the aforementioned buoy locations (see Fig. 11). RMS errors in magnitude and direction of Stokes drift estimates and the slope of fit m against $U_{\text{Spec}}^{\text{St}}$ are listed in Table 3.

In the SAB, Stokes drift estimates from pWW3 and pWW3 + E estimates of $S_{\eta\eta}(f, \theta)$ agree well with $U_{\text{Spec}}^{\text{St}}$ (see Table 3), while those from bWW3 are slightly less accurate (Fig. 11a). The UK MET approach slightly underestimates surface Stokes drift, while both the estimates from bulk formulations [Eq. (A.2)] are substantially smaller (Fig. 11a) with relatively large rms errors (see Table 3). Even though the bWW3 reconstruction-based Stokes drift estimates are reasonable in magnitude, the rms error in angle is $\approx 33.4°$ (see Table 3), which can have implications on defining the direction of passive tracers (i.e., oil or larval transport).

In the SCB, pWW3 + E provides the best $S_{\eta\eta}(f, \theta)$ estimates for surface Stokes drift (Fig. 11b) with rms errors 1.5 cm s^{-1} in magnitude and 10° in direction. The pWW3 estimates are also reasonably accurate as well (Table 3). Unlike in the SAB, in the SCB bWW3-based estimates of the surface Stokes drift magnitude and direction are poor (Table 3), potentially due to multipartitioned spectral peaks. UK MET Stokes drift exhibit slightly smaller rms errors than bWW3, while both bulk formula-based values underestimate the surface Stokes drift (Fig. 11b).

Overall, the exhaustive set of Stokes drift estimates using various methods presented here indicate that (i) any Stokes drift estimate using Eq. (A.1a) from reconstructed $S_{\eta\eta}(f, \theta)$ compares better than those from bulk parameter; (ii) estimates from reconstructed $S_{\eta\eta}(f, \theta)$ using standard parameters and energy at the peak period (i.e., pWW3 + E) appear to be overall the most accurate; (iii) in the SAB, even reconstructed $S_{\eta\eta}(f, \theta)$ using bulk wave parameters lead to accurate estimates of Stokes drift magnitude, but the direction can be incorrect; and (iv) even though UK MET approach best estimates the reconstructed $S_{\eta\eta}(f, \theta)$ (e.g., section 5a), it does not improve the accuracy of Stokes drift estimates. We suspect this is due to poor reconstruction of high-frequency spectra that weighs heavily on Stokes drift estimates.

Directional spreading at high frequency is large (e.g., Fig. 10), owing to the assumption of the reconstruction method that directional spread varies linearly as a function of frequency. The considerations for changing direction and directional spread as a function of frequency might not be linear and needs further improvements to avoid inaccuracies in Stokes drift estimates.

c. Recommendations for use in coupled wave–current model applications

Most coupled ocean circulation and wave propagation models studying wave–current interaction processes use bulk wave parameters to estimate regionally varying Stokes drift, often leading to incorrect vertical distribution (appendix A; Rascle et al. 2006; Gargett and Grosch 2014), which has implications for near-surface Lagrangian transport and upper-ocean turbulence. It is recommended that $S_{\eta\eta}(f, \theta)$-derived Stokes drift estimates be used, which may be achieved by estimating Stokes drift within the wave propagation model (e.g., Tolman 2014). Alternatively, the complete $S_{\eta\eta}(f, \theta)$ can be provided to the ocean circulation model, which is used to determine Stokes drift.

Also, partition-based, reconstructed $S_{\eta\eta}(f, \theta)$ open boundary condition for the spectral wave propagation model (e.g., SWAN) was more appropriate for regional, nearshore, downscaling applications, especially in regions with strong wave sheltering effects (see section 3b). The use of bulk wave parameter to simulate regional wave dynamics may lead to inaccurate local bulk wave and circulation parameters. Routine incorporation of the spectrum reconstruction methodology described in this work will benefit wave propagation and wave–current coupled circulation modeling significantly.

d. Recommendation for global wave modeling

Partitioning of complete $S_{\eta\eta}(f, \theta)$ and saving bulk wave parameters for each partition (Tracy et al. 2007) is an effective way to save space in storing hindcasts and forecasts from global wave model predictions, for example, WW3. The methodology presented here to reconstruct $S_{\eta\eta}(f, \theta)$

from partitioned data is robust enough for general use (sections 2a and 3b). Nonetheless, our analysis presented (see section 5a) suggests that the reconstruction process can be improved if at least $S_{\eta\eta}(f_p)$ is also added to the standard grid point output of global models. Usage of this parameter allows for better matching of the $S_{\eta\eta}(f, \theta)$ at peak frequency (section 5b). Inclusion of T_m, T_z, θ_p, and σ_p, as in Bunney et al. (2014), in the standard output suite can improve representation of skewed wind-sea conditions and may improve wave propagation accuracy in the nearshore, which requires further investigation. Reconstruction with these additional suggested parameters (UK MET) did not, however, improve the accuracy of Stokes drift estimates.

6. Conclusions

The implications of partitioned- and nonpartitioned-based directional wave spectrum $S_{\eta\eta}(f, \theta)$ as open boundary conditions for regional wave modeling are considered here. Key findings and recommendations from this study are as follows:

(i) Simulations using partitioned $S_{\eta\eta}(f, \theta)$ provide accurate regional wave parameter estimates (i.e., significant wave height, mean period, mean direction, and the directional spread) in comparison to nonpartition-based $S_{\eta\eta}(f, \theta)$ (see section 3b). It is strongly recommended that regional wave modeling studies use the publicly available partitioned WW3 hindcast/forecasts to reconstruct the complete directional spectrum for open boundary conditions.

(ii) Our methodology for the reconstruction of $S_{\eta\eta}(f, \theta)$ using partitioned bulk wave parameters provided by WW3 as standard output is suggested in setting open boundary conditions.

(iii) The reconstruction method as presented is suitable for improving HF radar–based surface Lagrangian current estimates as it allows for the correction of the radar-derived radial velocity for the missing Stokes drift value.

(iv) It is suggested that coupled ocean circulation and wave models estimate Stokes drift using formulations that take into account the complete $S_{\eta\eta}(f, \theta)$ (appendix A).

(v) Finally, it is recommended that global WW3 hindcast/ forecasts, in addition to storing the bulk wave parameters for each partition, also include the spectral energy at the peak frequency. The computational cost for estimating and storing this additional quantity is small, and it would improve the quality of the reconstructed directional spectra (section 5a) and surface Stokes drift estimates (section 5b) significantly.

APPENDIX A

Stokes Drift Estimates

Regional, coupled ocean circulation and wave propagation models estimate Stokes drift for calculating the total Lagrangian current and the Stokes production term for upper-ocean mixing. Stokes drift can be estimated either from bulk wave parameters or from complete $S_{\eta\eta}(f, \theta)$. For example,

$$
(u^{\text{St}}, v^{\text{St}})
$$
$$
= \int_{\theta=0}^{\theta=2\pi} \sigma k (\cos\theta, \sin\theta) S_{\eta\eta}(f, \theta) \frac{\cosh[2k(z+h)]}{\sinh^2(kh)} df\, d\theta,
$$

$$(\text{A.1a})$$

and

$$
(u^{\text{St}}, v^{\text{St}}) = \int_{\theta=0}^{\theta=2\pi} \sigma k S_{\eta\eta}(f) \frac{\cosh[2k(z+h)]}{\sinh^2(kh)} F(\theta)\, df\, d\theta,
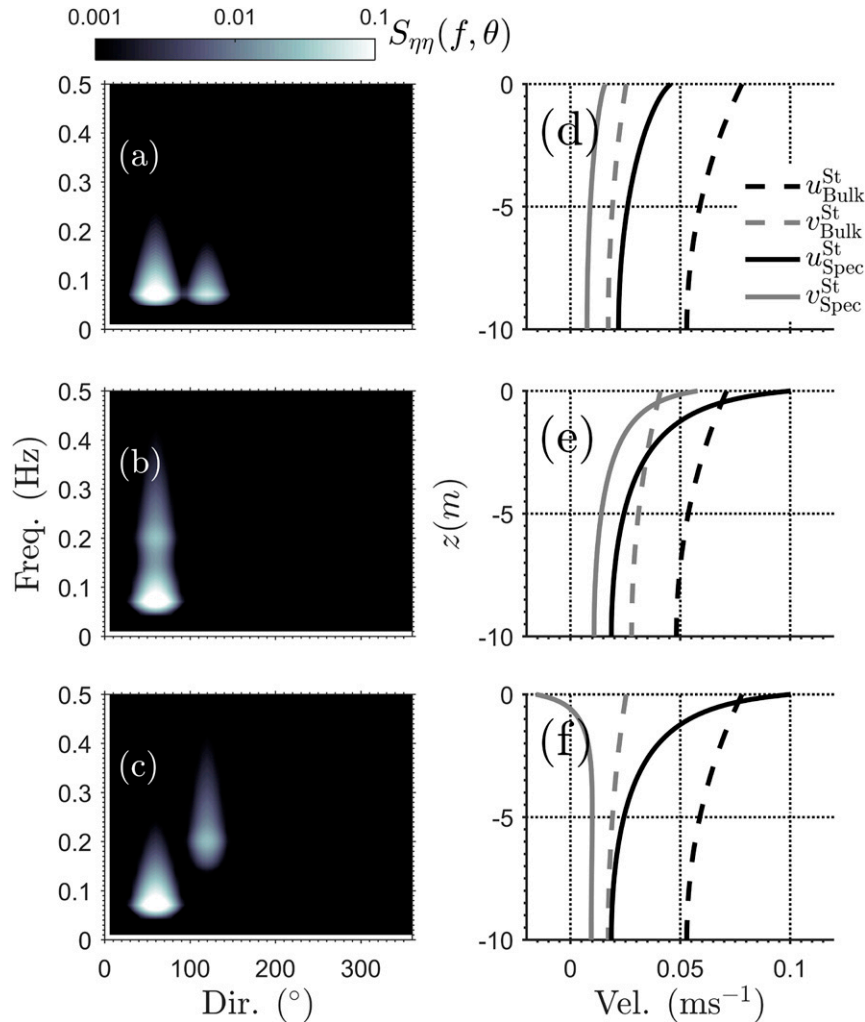$$

$$(\text{A.1b})$$

FIG. A1. Directional wave spectra $S_{\eta\eta}(f, \theta)$ (m^2 Hz^{-1} deg^{-1}) at $h = 10$ m for three cases corresponding to (a) unimodal, bidirectional; (b) bimodal, unidirectional; and (c) bimodal and bidirectional. North u^{St} (black) and east v^{St} (gray) Stokes drift as a function of water depth z estimated using spectral formulation [solid lines; Eq. (A.1a)] and bulk wave parameters [dashed lines; Eq. (A.2)].

while those from bulk wave parameters are shown as

$$(u^{\text{St}}, v^{\text{St}}) = \frac{H_s^2 \omega}{16} \frac{\cosh(2k_p(z + h))}{\sinh^2(k_p h)} k_p (\cos\theta, \sin\theta), \quad \text{(A.2)}$$

where z is the vertical coordinate, h is the water depth, θ is the wave direction, ω is angular wave frequency, k is the wavenumber related to ω through the dispersion relationship [i.e., $\omega^2 = gk \tanh(kh)$], and $F(\theta) = D(\theta)(\cos\theta, \sin\theta)$. At a constant wave frequency $\int_0^{2\pi} F(\theta) \sin\theta \, d\theta$ varies from 1 to 0.5 for directional spread from $\sigma_m = 0°$ to $45°$. Thus, a bulk wave forcing–based Stokes drift estimate [Eq. (A.2)] along the direction of wave propagation will be overestimated by a factor of 0.5–1 in comparison to spectral estimates [Eq. (A.1a)].

Here, three idealized $S_{\eta\eta}(f, \theta)$ (Figs. A1a–c) are considered. Each $S_{\eta\eta}(f, \theta)$ is created (method outlined in section 2b) by combination of two sets of partitioned bulk wave information (see Table A1). Bulk wave parameters (H_s, T_p, mean period T_m, mean direction θ_m, and mean directional spread σ_m; Table A1) for the combined $S_{\eta\eta}(f, \theta)$ (Fig. A1) are also estimated. Case A corresponds to a unimodal, bidirectional $S_{\eta\eta}(f, \theta)$ (see Table A1 and Fig. A1a); case B consists of a bimodal, unidirectional $S_{\eta\eta}(f, \theta)$ (Fig. A1b); and case C is a bimodal, bidirectional $S_{\eta\eta}(f, \theta)$ (Fig. A1c). The eastward u^{St} and northward v^{St} Stokes drift vertical profile at a water depth $h = 10$ m are estimated from Eqs. (A.1a) and (A.2).

For case A, spectral Stokes drift estimates (black and gray solid lines; Fig. A1d) are 50% of those estimated from

TABLE A1. List of partitioned and bulk wave parameters for cases A, B, and C.

Case	H_s	T_p	T_m	θ_m	σ_m
A					
Partition 1	2	14	8.6	60	10
Partition 2	1	14	8.6	120	10
Bulk	2.24	14	8.6	72	26
B					
Partition 1	2	14	8.6	60	10
Partition 2	1	5	3.9	60	10
Bulk	2.24	14	6.9	60	10
C					
Partition 1	2	14	8.6	60	10
Partition 2	1	5	3.9	120	10
Bulk	2.24	14	6.9	72	26

the bulk wave parameters (black and gray dashed lines, in Fig. A1d) for case A. In case B (Table A1), the eastward u^{St} and northward v^{St} Stokes drift from the spectral formulation equation [Eq. (A.1a)] are strongly sheared near surface in comparison to bulk estimate equation [Eq. (A.2)], while in deeper water the bulk estimates are stronger. These differences indicate that the upper-ocean mixing due to Stokes drift shear (e.g., McWilliams et al. 1997) would be underestimated when using bulk estimates. In case C, the eastward Stokes drift u^{St} from Eq. (A.1a) and Eq. (A.2) are the same as those estimates in case B, with stronger shear in spectral estimates in comparison to bulk estimates (cf. black solid and dashed lines in Fig. A1f). The northward Stokes drift v^{St} from the complete spectrum is negligible throughout the water column, as v^{St} from first partition partially cancels v^{St} from the second partition. The bulk formula [Eq. (A.2)] uses the bulk estimate of mean direction ($\theta_m = 72°$) and overestimates v^{St} with magnitude 5 times those obtained from Eq. (A.1a) (cf. solid and dashed gray line Fig. A1f).

APPENDIX B

Relevant Metrics

Here, relevant metrics for the estimation of bulk quantities from the $S_{\eta\eta}(f, \theta)$ are provided:

$$S_{\eta\eta}(\theta) = \int_{f=0}^{f=1} S_{\eta\eta}(f, \theta)\, df, \tag{B.1}$$

$$H_s = 4\sqrt{\int_{f=0}^{f=1} \int_{\theta=0}^{\theta=2\pi} S_{\eta\eta}(f, \theta)\, d\theta\, df}, \tag{B.2}$$

$$T_m = \frac{\int_0^1 S_{\eta\eta}(f)\, df}{\int_0^1 f S_{\eta\eta}(f)\, df}, \tag{B.3}$$

$$\theta_m = \frac{\int_0^{2\pi} \theta S_{\eta\eta}(\theta)\, d\theta}{\int_0^{2\pi} S_{\eta\eta}(\theta)\, d\theta}, \quad \text{and} \tag{B.4}$$

$$\sigma_\theta = \sqrt{\frac{\int_{f=0}^{f=1}\left[\int_0^{2\pi} (\theta - \theta_m)^2 D(\theta)\, d\theta\right] S_{\eta\eta}(f)\, df}{\int_{f=0}^{f=1} S_{\eta\eta}(f)\, df}}. \tag{B.5}$$

REFERENCES

Adams, P. N., D. L. Inman, and N. E. Graham, 2008: Southern California deep-water wave climate: Characterization and application to coastal processes. *J. Coastal Res.*, **24**, 1022–1035, doi:10.2112/07-0831.1.

Ardhuin, F., N. Rascle, and K. A. Belibassakis, 2008: Explicit wave-averaged primitive equations using a generalized Lagrangian mean. *Ocean Modell.*, **20**, 35–60, doi:10.1016/j.ocemod.2007.07.001.

——, L. Marié, N. Rascle, P. Forget, and A. Roland, 2009: Observation and estimation of Lagrangian, Stokes, and Eulerian currents induced by wind and waves at the sea surface. *J. Phys. Oceanogr.*, **39**, 2820–2838, doi:10.1175/2009JPO4169.1.

Barnard, P. L., M. van Ormondt, L. H. Erikson, J. Eshleman, C. Hapke, P. Ruggiero, P. N. Adams, and A. C. Foxgrover, 2014: Development of the Coastal Storm Modeling System (CoSMoS) for predicting the impact of storms on high-energy, active-margin coasts. *Nat. Hazards*, **74**, 1095–1125, doi:10.1007/s11069-014-1236-y.

Barrick, D., and B. Weber, 1977: On the nonlinear theory for gravity waves on the ocean's surface. Part II: Interpretation and applications. *J. Phys. Oceanogr.*, **7**, 11–21, doi:10.1175/1520-0485(1977)007<0011:OTNTFG>2.0.CO;2.

Bennis, A.-C., F. Ardhuin, and F. Dumas, 2011: On the coupling of wave and three-dimensional circulation models: Choice of theoretical framework, practical implementation and adiabatic tests. *Ocean Modell.*, **40**, 260–272, doi:10.1016/j.ocemod.2011.09.003.

Booij, N., R. Ris, and L. H. Holthuijsen, 1999: A third-generation wave model for coastal regions: 1. Model description and validation. *J. Geophys. Res.*, **104**, 7649–7666, doi:10.1029/98JC02622.

Breivik, Ø., and Ø. Sætra, 2001: Real time assimilation of HF radar currents into a coastal ocean model. *J. Mar. Syst.*, **28**, 161–182, doi:10.1016/S0924-7963(01)00002-1.

——, J.-R. Bidlot, and P. A. Janssen, 2016: A Stokes drift approximation based on the Phillips spectrum. *Ocean Modell.*, **100**, 49–56, doi:10.1016/j.ocemod.2016.01.005.

Broche, P., J. Demaistre, and P. Forget, 1983: Mesure par radar décamétrique cohérent des courants superficiels engendrés par le vent. *Oceanol. Acta*, **6**, 43–53.

Broström, G., A. Carrasco, L. Hole, S. Dick, F. Janssen, J. Mattsson, and S. Berger, 2011: Usefulness of high resolution coastal models for operational oil spill forecast: The "Full City" accident. *Ocean Sci.*, **7**, 805–820, doi:10.5194/os-7-805-2011.

Bunney, C., A. Saulter, and T. Palmer, 2014: Reconstruction of complex 2D wave spectra for rapid deployment of nearshore wave models. *From Sea to Shore—Meeting the Challenges of the Sea (Coasts, Marine Structures and Breakwaters 2013)*, W. Allsop and K. Burgess, Eds., 1050–1059.

Cahl, D. L., and G. Voulgaris, 2016: HF radar Lagrangian trajectory calculations accounting for Stokes drift and the nonlinear Bragg wave phase speed correction term. *Extended Abstracts, 2016 Ocean Sciences Meeting*, New Orleans, LA, ASLO, eC44B-1247. [Available online at https://agu.confex.com/agu/os16/preliminaryview.cgi/Paper92023.html.]

Chawla, A., D. M. Spindler, and H. L. Tolman, 2013: Validation of a thirty year wave hindcast using the Climate Forecast System Reanalysis winds. *Ocean Modell.*, **70**, 189–206, doi:10.1016/j.ocemod.2012.07.005.

Craik, A., and S. Leibovich, 1976: A rational model for Langmuir circulations. *J. Fluid Mech.*, **73**, 401–426, doi:10.1017/S0022112076001420.

Crombie, D. D., 1955: Doppler spectrum of sea echo at 13.56 Mc./s. *Nature*, **175**, 681–682, doi:10.1038/175681a0.

Crosby, S. C., W. C. O'Reilly, and R. T. Guza, 2016: Modeling long period swell in Southern California: Practical boundary conditions from buoy observations and global wave model predictions. *J. Atmos. Oceanic Technol.*, **33**, 1673–1690, doi:10.1175/JTECH-D-16-0038.1.

D'Asaro, E. A., 2014: Turbulence in the upper-ocean mixed layer. *Annu. Rev. Mar. Sci.*, **6**, 101–115, doi:10.1146/annurev-marine-010213-135138.

Ewans, K. C., 1998: Observations of the directional spectrum of fetch-limited waves. *J. Phys. Oceanogr.*, **28**, 495–512, doi:10.1175/1520-0485(1998)028<0495:OOTDSO>2.0.CO;2.

Gargett, A., and C. Grosch, 2014: Turbulence process domination under the combined forcings of wind stress, the Langmuir vortex force, and surface cooling. *J. Phys. Oceanogr.*, **44**, 44–67, doi:10.1175/JPO-D-13-021.1.

Hanson, J. L., and O. M. Phillips, 2001: Automated analysis of ocean surface directional wave spectra. *J. Atmos. Oceanic Technol.*, **18**, 277–293, doi:10.1175/1520-0426(2001)018<0277:AAOOSD>2.0.CO;2.

——, and R. E. Jensen, 2004: Wave system diagnostics for numerical wave models. *Proc. Eighth Int. Workshop on Wave Hindcasting and Forecasting*, North Shore, Oahu, HI, U.S. Army Corps of Engineers, Coastal and Hydraulics Laboratory, E3. [Available online at http://www.waveworkshop.org/8thWaves/Papers/E3.pdf.]

Harlan, J., E. Terrill, L. Hazard, C. Keen, D. Barrick, C. Whelan, S. Howden, and J. Kohut, 2010: The integrated ocean observing system high-frequency radar network: Status and local, regional, and national applications. *Mar. Technol. Soc. J.*, **44**, 122–132, doi:10.4031/MTSJ.44.6.6.

Hasselmann, K., and Coauthors, 1973: Measurements of wind-wave growth and swell decay during the Joint North Sea Wave Project (JONSWAP). *Dtsch. Hydrogr. Z.*, **8A** (Suppl.), 95 pp.

Herbers, T., S. Elgar, and R. T. Guza, 1999: Directional spreading of waves in the nearshore. *J. Geophys. Res.*, **104**, 7683–7693, doi:10.1029/1998JC900092.

Hopkins, J., S. Elgar, and B. Raubenheimer, 2016: Observations and model simulations of wave-current interaction on the inner shelf. *J. Geophys. Res. Oceans*, **121**, 198–208, doi:10.1002/2015JC010788.

Kenyon, K. E., 1969: Stokes drift for random gravity waves. *J. Geophys. Res.*, **74**, 6991–6994, doi:10.1029/JC074i028p06991.

Kuik, A. J., G. P. V. Vledder, and L. H. Holthuijsen, 1988: A method for the routine analysis of pitch-and-roll buoy wave data. *J. Phys. Oceanogr.*, **18**, 1020–1034, doi:10.1175/1520-0485(1988)018<1020:AMFTRA>2.0.CO;2.

Kumar, N., G. Voulgaris, J. C. Warner, and M. Olabarrieta, 2012: Implementation of the vortex force formalism in the Coupled Ocean-Atmosphere-Wave-Sediment Transport (COAWST) modeling system for inner shelf and surf zone applications. *Ocean Modell.*, **47**, 65–95, doi:10.1016/j.ocemod.2012.01.003.

Lentz, S. J., M. Fewings, P. Howd, J. Fredericks, and K. Hathaway, 2008: Observations and a model of undertow over the inner continental shelf. *J. Phys. Oceanogr.*, **38**, 2341–2357, doi:10.1175/2008JPO3986.1.

Liu, Y., R. H. Weisberg, and C. R. Merz, 2014: Assessment of CODAR SeaSonde and WERA HF radars in mapping surface currents on the west Florida shelf. *J. Atmos. Oceanic Technol.*, **31**, 1363–1382, doi:10.1175/JTECH-D-13-00107.1.

Long, C. E., and D. T. Resio, 2007: Wind wave spectral observations in Currituck Sound, North Carolina. *J. Geophys. Res.*, **112**, C05001, doi:10.1029/2006JC003835.

Longuet-Higgins, M. S., D. Cartwright, and N. Smith, 1961: Observations of the directional spectrum of sea waves using the motions of a floating buoy. *Ocean Wave Spectra: Proceedings of a Conference*, Prentice-Hall, 111–132.

McWilliams, J. C., P. P. Sullivan, and C.-H. Moeng, 1997: Langmuir turbulence in the ocean. *J. Fluid Mech.*, **334**, 1–30, doi:10.1017/S0022112096004375.

Mitsuyasu, H., F. Tasai, T. Suhara, S. Mizuno, M. Ohkusu, T. Honda, and K. Rikiishi, 1975: Observations of the directional spectrum of ocean waves using a cloverleaf buoy. *J. Phys. Oceanogr.*, **5**, 750–760, doi:10.1175/1520-0485(1975)005<0750:OOTDSO>2.0.CO;2.

Moghimi, S., K. Klingbeil, U. Gräwe, and H. Burchard, 2013: A direct comparison of a depth-dependent radiation stress formulation and a vortex force formulation within a three-dimensional coastal ocean model. *Ocean Modell.*, **70**, 132–144, doi:10.1016/j.ocemod.2012.10.002.

Ochoa, J., and O. E. Delgado-González, 1990: Pitfalls in the estimation of wind wave directional spectra by variational principles. *Appl. Ocean Res.*, **12**, 180–187, doi:10.1016/S0141-1187(05)80025-2.

Olabarrieta, M., J. C. Warner, B. Armstrong, J. B. Zambon, and R. He, 2012: Ocean–atmosphere dynamics during Hurricane Ida and Nor'Ida: An application of the Coupled Ocean–Atmosphere–Wave–Sediment Transport (COAWST) modeling system. *Ocean Model.*, **43–44**, 112–137, doi:10.1016/j.ocemod.2011.12.008.

O'Reilly, W., and R. T. Guza, 1991: Comparison of spectral refraction and refraction-diffraction wave models. *J. Waterw. Port Coastal Ocean Eng.*, **117**, 199–215, doi:10.1061/(ASCE)0733-950X(1991)117:3(199).

——, and ——, 1993: A comparison of two spectral wave models in the Southern California Bight. *Coastal Eng.*, **19**, 263–282, doi:10.1016/0378-3839(93)90032-4.

——, C. B. Olfe, J. Thomas, R. Seymour, and R. Guza, 2016: The California coastal wave monitoring and prediction system. *Coastal Eng.*, **116**, 118–132, doi:10.1016/j.coastaleng.2016.06.005.

Paduan, J. D., and I. Shulman, 2004: HF radar data assimilation in the Monterey Bay area. *J. Geophys. Res.*, **109**, C07S09, doi:10.1029/2003JC001949.

——, and L. Washburn, 2013: High-frequency radar observations of ocean surface currents. *Annu. Rev. Mar. Sci.*, **5**, 115–136, doi:10.1146/annurev-marine-121211-172315.

Pawka, S., D. Inman, and R. Guza, 1984: Island sheltering of surface gravity waves: Model and experiment. *Cont. Shelf Res.*, **3**, 35–53, doi:10.1016/0278-4343(84)90042-6.

Pierson, W. J., Jr., and L. Moskowitz, 1964: A proposed spectral form for fully developed wind seas based on the similarity theory of S. A. Kitaigorodskii. *J. Geophys. Res.*, **69**, 5181–5190, doi:10.1029/JZ069i024p05181.

Rascle, N., and F. Ardhuin, 2013: A global wave parameter database for geophysical applications. Part 2: Model validation with improved source term parameterization. *Ocean Modell.*, **70**, 174–188, doi:10.1016/j.ocemod.2012.12.001.

——, ——, and E. A. Terray, 2006: Drift and mixing under the ocean surface: A coherent one-dimensional description with application to unstratified conditions. *J. Geophys. Res.*, **111**, C03016, doi:10.1029/2005JC003004.

——, ——, P. Queffeulou, and D. Croizé-Fillon, 2008: A global wave parameter database for geophysical applications. Part 1: Wave-current–turbulence interaction parameters for the open ocean based on traditional parameterizations. *Ocean Modell.*, **25**, 154–171, doi:10.1016/j.ocemod.2008.07.006.

Ris, R., L. Holthuijsen, and N. Booij, 1999: A third-generation wave model for coastal regions: 2. Verification. *J. Geophys. Res.*, **104**, 7667–7681, doi:10.1029/1998JC900123.

Rogers, W. E., J. M. Kaihatu, L. Hsu, R. E. Jensen, J. D. Dykes, and K. T. Holland, 2007: Forecasting and hindcasting waves with the swan model in the Southern California Bight. *Coastal Eng.*, **54**, 1–15, doi:10.1016/j.coastaleng.2006.06.011.

Röhrs, J., K. H. Christensen, F. Vikebø, S. Sundby, Ø. Saetra, and G. Broström, 2014: Wave-induced transport and vertical mixing of pelagic eggs and larvae. *Limnol. Oceanogr.*, **59**, 1213–1227, doi:10.4319/lo.2014.59.4.1213.

Rypina, I. I., A. R. Kirincich, R. Limeburner, and I. A. Udovydchenkov, 2014: Eulerian and Lagrangian correspondence of high-frequency radar and surface drifter data: Effects of radar resolution and flow components. *J. Atmos. Oceanic Technol.*, **31**, 945–966, doi:10.1175/JTECH-D-13-00146.1.

Stokes, G. G., 1847: On the theory of oscillatory waves. *Trans. Cambridge Philos. Soc.*, **8**, 441–473.

Tejada-Martínez, A. E., and C. E. Grosch, 2007: Langmuir turbulence in shallow water. Part 2. Large-eddy simulation. *J. Fluid Mech.*, **576**, 63–108, doi:10.1017/S0022112006004587.

Tolman, H. L., 2009: User manual and system documentation of WAVEWATCH III TM version 3.14. Environmental Modeling Center, Marine Modeling and Analysis Branch Contribution 276, 220 pp.

——, 2014: User manual and system documentation of WAVEWATCH III version 4.18. WAVEWATCH III Development Group, Environmental Modeling Center, Marine Modeling and Analysis Branch Contribution 316, 311 pp.

Tracy, B., E. Devaliere, J. Hanson, T. Nicolini, and H. Tolman, 2007: Wind sea and swell delineation for numerical wave modeling. *Proc. 10th Int. Workshop on Wave Hindcasting and Forecasting Coastal Hazard Symp.*, North Shore, Oahu, HI, U.S. Army Engineer Research and Development Center, P12. [Available online at http://www.waveworkshop.org/10thWaves/ProgramFrameset.htm.]

Uchiyama, Y., J. C. McWilliams, and A. F. Shchepetkin, 2010: Wave–current interaction in an oceanic circulation model with a vortex-force formalism: Application to the surf zone. *Ocean Modell.*, **34**, 16–35, doi:10.1016/j.ocemod.2010.04.002.

Ullman, D. S., J. O'Donnell, J. Kohut, T. Fake, and A. Allen, 2006: Trajectory prediction using HF radar surface currents: Monte Carlo simulations of prediction uncertainties. *J. Geophys. Res.*, **111**, C12005, doi:10.1029/2006JC003715.

Vincent, L., and P. Soille, 1991: Watersheds in digital spaces: An efficient algorithm based on immersion simulations. *IEEE Trans. Pattern Anal. Mach. Intell.*, **13**, 583–598, doi:10.1109/34.87344.

Wang, D. W., and P. A. Hwang, 2001: Evolution of the bimodal directional distribution of ocean waves. *J. Phys. Oceanogr.*, **31**, 1200–1221, doi:10.1175/1520-0485(2001)031<1200:EOTBDD>2.0.CO;2.

Warner, J. C., B. Armstrong, R. He, and J. B. Zambon, 2010: Development of a Coupled Ocean–Atmosphere–Wave–Sediment Transport (COAWST) modeling system. *Ocean Modell.*, **35**, 230–244, doi:10.1016/j.ocemod.2010.07.010.

Webb, A., and B. Fox-Kemper, 2015: Impacts of wave spreading and multidirectional waves on estimating stokes drift. *Ocean Modell.*, **96**, 49–64, doi:10.1016/j.ocemod.2014.12.007.